#### **Research Article**

Fahad A. Alharthi\*, Mohammed Abdullah Albaeejan, Alanoud Abdullah Alshayiqi, Hend Khalid Aldubeikl, and Imran Hasan\*

# Enhanced visible-light-driven photocatalytic degradation of azo dyes by heteroatom-doped nickel tungstate nanoparticles

https://doi.org/10.1515/ntrev-2023-0143 received March 14, 2023; accepted October 2, 2023

Abstract: In this study, we conducted the hydrothermal synthesis of cobalt (Co)-doped NiWO<sub>4</sub>, resulting in the formation of Co-NiWO<sub>4</sub> nanoparticles (NPs), followed by calcination at 550°C for 12 h. Comprehensive analyses were performed to characterize the composition, structure, and morphology of the synthesized material. X-ray diffraction results confirmed the successful inclusion of Co in the NiWO<sub>4</sub> lattice, with the presence of characteristic peaks of CoWO<sub>4</sub>. The crystallite size, determined using the Scherrer equation, was measured to be 22 nm. Using UV-Vis spectroscopy and Tauc's equation, we calculated the band gap energy ( $E_g$ ) to be 3.75 eV for NiWO<sub>4</sub> and 1.75 eV for Co-NiWO<sub>4</sub>. The potential application of the synthesized material as a photocatalyst was investigated for the degradation of the diazo dye Congo red (CR). Under optimized reaction conditions, Co-NiWO<sub>4</sub> NPs demonstrated outstanding efficiency, degrading a total of 95% of CR. The degradation kinetics were well-described by the Langmuir-Hinshelwood (L-H) kinetic model, indicating that photoabsorption played a crucial role in the rate-controlling step. These encouraging results suggest that Co-NiWO<sub>4</sub> NPs hold promise as a viable option for addressing other pollutants in various applications.

**Mohammed Abdullah Albaeejan:** Department of Chemistry, College of Science, King Saud University, Riyadh-11451, Saudi Arabia, e-mail: mohmdasb01@gmail.com

**Alanoud Abdullah Alshayiqi:** Department of Chemistry, College of Science, King Saud University, Riyadh-11451, Saudi Arabia, e-mail: alanoud.alshayiqi@gmail.com

**Hend Khalid Aldubeikl:** Department of Chemistry, College of Science, King Saud University, Riyadh-11451, Saudi Arabia, e-mail: HK.Aldubeikl@gmail.com

**Keywords:** semiconductor photocatalysis, nanocomposites, hydrothermal synthesis, monoclinic structure, photoabsorption

# 1 Introduction

In the current context of robust globalization and industrial growth, the decline in clean water quality is evident, primarily due to the introduction of hazardous pollutants like heavy metals and dyes from direct and indirect sources [1,2]. Azo dyes, a group of synthetic compounds containing one or more azo groups (-N=N-) as chromophores, are particularly noteworthy among these pollutants [3,4]. Their distinctive colors, ease of synthesis, high solubility, and excellent fastness rating make them favored colorants in industries such as food, pharmaceuticals, and textiles [5,6]. However, despite their advantageous properties, azo dyes are known to be toxic, allergenic to human skin, and carcinogenic, leading to strict regulations governing their use in many countries [7,8]. One specific azo dye of concern is Congo red (CR), an anionic bis azo dye containing benzidine salt, which poses a significant health risk due to its tendency to bioaccumulate in the human body and contribute to various neurological and respiratory ailments [1,9]. Therefore, there is a pressing need to develop efficient and environmentally friendly methods and materials capable of effectively degrading the CR dye in wastewater before its release into water bodies or the environment.

The literature presents various methods for CR removal from wastewater, including biodegradation, ultrafiltration, adsorption, and chemical oxidation. However, the production of secondary-level sludge, the generation of pollutants, and complex operational procedures have limited their practical application [10,11]. To address these challenges, a promising approach is the photocatalysis-based advanced oxidation process. This method harnesses solar light to interact with a catalyst material, leading to the generation of electron—hole  $(e^-/h^+)$  pairs. These active  $e^-/h^+$  pairs effectively attack CR

<sup>\*</sup> Corresponding author: Fahad A. Alharthi, Department of Chemistry, College of Science, King Saud University, Riyadh-11451, Saudi Arabia, e-mail: fharthi@ksu.edu.sa

<sup>\*</sup> Corresponding author: Imran Hasan, Department of Chemistry, College of Science, King Saud University, Riyadh-11451, Saudi Arabia, e-mail: iabdulateef@ksu.edu.sa

molecules, breaking them into smaller, non-toxic compounds such as  $CO_2$  and  $H_2O$  [12,13]. Designing materials with the ability to efficiently generate and stabilize these  $e^-/h^+$  pairs is crucial for the success of this eco-friendly and sustainable process.

Various semiconductor-based nanomaterials have been synthesized and used as photocatalysts for the degradation of CR such as V<sub>2</sub>O<sub>5</sub>-TiO<sub>2</sub>, ZnO, plasmonic metal nanoparticles (NPs) (Ag, Au, Pd, and Pt), ZnO-ZnS-CdO-CdS, ZnS:Fe, Fe<sub>2</sub>(MoO<sub>4</sub>)<sub>3.</sub> etc. [14-19]. Among all these metal oxide and metal sulfide NPs, a high rate of charge recombination and wide band gap hinders the efficiency of TiO<sub>2</sub>, the agueous medium instability of ZnO NPs at variational pH values, toxic sulfide release under illumination rules out the utilization of sulfide catalyst water decontamination [14,17,18]. These discrepancies between metal oxide and sulfide NPs draw the attention of scientists and researchers toward the utilization of multi-metal component-based photocatalytic materials. The materials, such as SrTiO<sub>3</sub> [20], NaTaO<sub>3</sub> [21], BaTi<sub>4</sub>O<sub>9</sub> [22], CaIn<sub>2</sub>O<sub>4</sub> [23], and La<sub>1-X</sub>Cr<sub>x</sub>FeO<sub>3</sub> [24], have been reported to decontaminate wastewater

One of the classes of multi-metal-based oxide attracting the attention of the scientific community is tungstate-based nanomaterials with the empirical formula  $MWO_4$  (M = Co, Ni, Cu, and Fe) [25,26]. They have been proven to be a promising agent for environmental decontamination and solar water splitting due to narrow band gaps with extraordinary light absorption quality [27,28]. They are widely applied in various industrial processes such as scintillation, microwave technology, fiber optics, catalysis, and photoluminescence [29,30]. Among all these, NiWO<sub>4</sub> with an energy band gap value of 2.6 eV is one of the important tungstate family members having very high demands in fields like laser hosts, humidity sensors, catalysis, and microwave application [31]. Appreciable work has been reported in the literature corresponding to the utilization of ZnWO4 as a photocatalyst toward the degradation of toxic dyes and amplification in photocatalytic efficiency through hetero atom doping [32–35]. The photocatalytic behavior of other tungstate materials such as PbWO4 and Bi2WO4 was also explored in the literature [36,37]. However, no studies are reported in the literature regarding the utilization of Co-doped NiWO<sub>4</sub> NPs toward photocatalytic degradation of CR. Therefore, this research gap provides the opportunity to elaborate the information regarding variations in the structural, morphological, optical, and photocatalytic properties of Co-doped NiWO<sub>4</sub>. Although pristine NiWO<sub>4</sub> exhibits very good photocatalytic performances for the mineralization of organic contaminants, however, because of its high purity, the high e<sup>-</sup>/h<sup>+</sup> recombination rate limits its photocatalytic efficiency [30]. To address these issues and improve the overall

catalytic performance of NiWO<sub>4</sub>, various chemical techniques such as semiconductor coupling, [31], doping [29], noble metal deposition [35], and morphology control [30] were considered. In the present study, the method of doping with a suitable metal atom in the pure crystal lattice of NiWO<sub>4</sub> was chosen to reflect changes in the structural matrix to achieve the required optical properties. From the literature, various studies have been reported on the metal doping of NiWO<sub>4</sub> for multidisciplinary applications such as Cu doping, Mn doping, Bi doping, etc. [38-40]. In this study, cobalt (Co<sup>2+</sup>) was specifically chosen as a dopant due to its similar ionic radius and strong magnetic moment (μCo = 1.8 μB d7 low spin configuration) [41,42]. By introducing Co<sup>2+</sup> into the NiWO<sub>4</sub> solid matrix, we aimed to inhibit e<sup>-</sup>/h<sup>+</sup> recombination and enhance photocatalytic activities via Ni d-d transitions and Co-W metal charge transfer mechanisms [43]. Several methods have been reported in the literature for synthesizing NiWO<sub>4</sub> and mixed metalbased tungstate nanomaterials, including sol-gel processing [44], solid-state reaction [45], a hydrothermal method [46], and polymerized complex method [47]. These methods have shown enhanced stability, improved electron transport mechanisms, and higher energy density in the resulting nanostructures. In this study, we employed a hydrothermal route to synthesize pure phase (Co, Ni, Cu, Zn)-tungstates with a uniform particle size distribution, and we explored their potential as a photocatalyst for degrading the diazo dye CR. Additionally, we investigated the impact of various reaction parameters, such as irradiation time (minutes), pH, catalyst dose, visible light intensity, temperature, and leaching experiments, on the photocatalytic efficiency of Co-NiWO<sub>4</sub> NPs in degrading CR. These investigations aimed to understand the factors influencing the photocatalytic process and optimize the performance of Co-NiWO<sub>4</sub> NPs as an effective photocatalyst for CR degradation.

# 2 Materials and methods

#### 2.1 Chemicals

Sodium tungstate dehydrate ( $Na_2WO_4$ : $2H_2O$ , 98%) was purchased from Loba Chemie. Nickel nitrate hexahydrate (Ni ( $NO_3$ )<sub>2</sub>: $6H_2O$ , 98%) and cobalt nitrate hexahydrate (Co ( $NO_3$ )<sub>2</sub>: $6H_2O$ , 98%) were purchased from Merck. CR (99%) and ammonia solution (25%) were purchased from Otto Chemie. Double distilled water was used throughout the experiments, and the chemicals received were used as such without any further purification (Figure 1).

# 2.2 Preparation of the Co-NiWO<sub>4</sub> nanocomposite

The pristine NiWO<sub>4</sub> and Co-NiWO<sub>4</sub> NPs were synthesized using the hydrothermal method as described in a previous study [46]. To prepare the NPs, a solution containing equimolar (1:1) amounts of Ni (NO<sub>3</sub>)<sub>2</sub>·6H<sub>2</sub>O and Co (NO<sub>3</sub>)<sub>2</sub>·6H<sub>2</sub>O (both 5 mmol) was prepared in 25 mL of deionized (DI) water and stirred for 1h at 25°C until a clear solution was obtained. This solution was labeled as Solution A. Next, Solution A was added dropwise to a 10 mmol solution of Na<sub>2</sub>WO<sub>4</sub>·2H<sub>2</sub>O (Solution B). The resulting mixture was stirred on a magnetic stirrer until homogeneity was achieved. To maintain the pH ~8–10, 10 mL of a 25% ammonia solution was added to the mixture (Solution A + Solution B). After 30 min of stirring, the mixture was transferred to a 100 mL Teflon-lined autoclave and placed in a digital oven at 190°C for 12 h for the hydrothermal treatment. Subsequently, the material was obtained by centrifugation and washed multiple times with DI water until the effluents exhibited a neutral pH. The washed material was then dehydrated in an oven at 100°C for 6 h and subsequently calcined at 500°C for 4 h under an N<sub>2</sub> atmosphere.

#### 2.3 Material characterization

Various analytical techniques were employed to characterize the synthesized material and confirm the successful formation of the desired Co–NiWO<sub>4</sub> nanocomposite. Fourier transform infrared spectroscopy (FTIR) was used to investigate the bond formation between Co and WO<sub>4</sub><sup>2-</sup> and the peak shifting upon Co inclusion in the NiWO<sub>4</sub> matrix, with measurements taken in the range of 4,000–400 cm<sup>-1</sup> using a Perkin Elmer Spectrum 2 ATR spectrometer. The X-ray diffraction (XRD) method, conducted with a Rigaku Ultima 1 V X-ray diffractometer, provided insights into changes in the lattice, crystallite size, and interplanar distance resulting from Co doping in the NiWO<sub>4</sub> crystal lattice. Scanning electron microscopy (SEM) in conjunction with energy X-ray

$$NH_{2} \qquad NH_{3}C \qquad CH_{3} \qquad NH_{2}$$

$$N=N \qquad N=N$$

$$SO_{3}Na^{+}$$

$$Congo Red$$

Figure 1: Chemical structure of the CR dye.

diffraction (EDX) and mapping (JEOL GSM 6510LV, Japan) were utilized to study the surface morphology and elemental composition of the synthesized material. Transmission electron microscopy (TEM) using a JEM 2100 microscope (Japan) allowed the observation of variations in the crystallite size and crystal structure after solid-state reactions. To analyze the electron shift occurring upon Co doping and to assess the concentration of CR remaining after the photocatalytic experiment, ultraviolet-visible spectroscopy (UV-Vis) was employed with a Shimadzu UV-1900 spectrophotometer. These comprehensive characterizations contributed to a thorough understanding of the material's properties and its potential application as an efficient photocatalyst for CR degradation.

# 2.4 Photocatalytic activity

The photocatalytic performance of the as-synthesized nanocomposite material as a catalyst was evaluated by studying the degradation of CR (30, 50, and 70 ppm) under visible solar radiation. An aliquot of 10 mL of 20 ppm CR dye was treated with 10 mg of Co–NiWO<sub>4</sub> NPs sonicated for 3 min and then placed under dark for 1 h to maintain absorption–desorption equilibrium. Then, the mixture was placed under visible light radiation (350 W, Xe lamp with 100 mW cm<sup>-2</sup> intensity,  $\lambda > 420$  nm) for an optimum amount of time, and the concentration of CR post-reaction was assessed by taking 3 mL of aliquot using UV–Vis spectrophotometer at  $\lambda_{\rm max} = 494$  nm. All the experiments were repeated three times to get better precision and suppress maximum error in the data. The photocatalytic efficiency of Co–NiWO<sub>4</sub> NPs toward the CR dye was evaluated by the following equation:

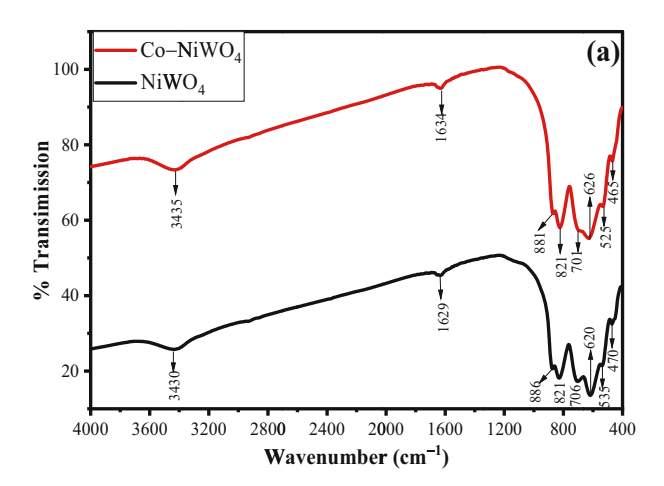
Degradation (%) = 
$$\left(\frac{C_0 - C_e}{C_o}\right) \times 100$$
, (1)

where  $C_0$  and  $C_e$  are the concentration of CR at the initial state and each time interval, respectively.

# 3 Results and discussion

#### 3.1 Material characterization

Figure 2(a) displays the FTIR spectra of NiWO<sub>4</sub>, CoWO<sub>4</sub>, and Co–NiWO<sub>4</sub> NPs in which pristine NiWO<sub>4</sub> shows the characteristic peaks at 470 cm<sup>-1</sup> (stretching vibrations of Ni–O bond), 535 cm<sup>-1</sup> (W–O bonds), 620 and 706 cm<sup>-1</sup> (bending



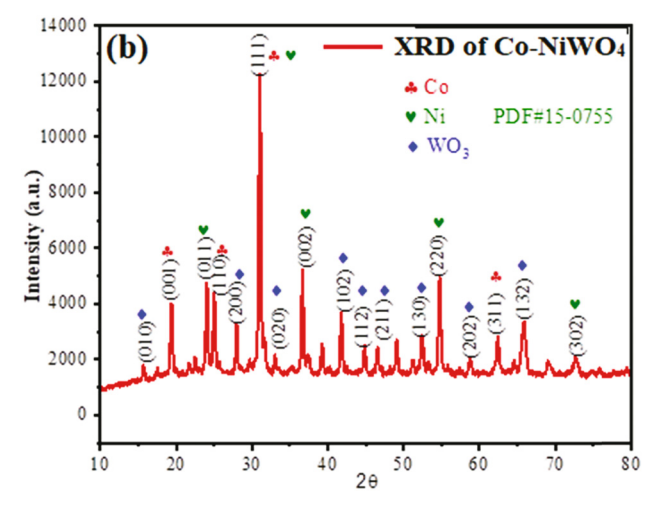


**Figure 2:** (a) FTIR of NiWO $_4$  (black line), CoWO $_4$  (red line), and Co-NiWO $_4$  NPs (red line). (b) XRD spectra of NiWO $_4$  (red line) and Co-NiWO $_4$  NPs (blue line).

and stretching vibrations of W–O bond in  $WO_6^{\,6-}$  octahedron), and 821 and 886 cm<sup>-1</sup> (bending and stretching vibration of the  $WO_2$  entity associated with  $W_2O_8$  groups) [48]. In addition, the peaks at 3,430 and 1,629 cm<sup>-1</sup> (stretching and bending vibrations of –OH groups) suggest the presence of a notable amount of surface-adsorbed water. The FTIR spectra of Co–NiWO<sub>4</sub> NPs reveal all the peaks like pristine NiWO<sub>4</sub> with some shifted values due to doping of Co in the solid lattice. The observed absorption bands are in good agreement with IR data on NiWO<sub>4</sub> with the wolframite structure [43,49].

Figure 2(b) shows the XRD spectra of as-synthesized Co–NiWO<sub>4</sub> NPs, which exhibit the characteristic peaks at  $2\theta$  values of 15.62, 19.45, 24.03, 25.05, 27.86, 30.92, 32.96, 36.45, 41.75, 44.92, 46.71, 52.45, 54.62, 58.81, 62.39, 65.95, and 72.84° corresponding to Miller indices values of (010), (001), (011), (110), (200), (111), (020), (002), (102), (112), (211), (130), (132), and (302) (JCPDS No. 15-0755), respectively. From the literature, the Miller indices values for pure

NiWO<sub>4</sub> have been reported as (010), (100), (011), (110), (111), (021), (200), (121), (112), (211), (022), (220), (130), (202), (113), (311), and (041) with wolframite monoclinic structure associated with JCPDS No. 72-0480. Based on the Miller indices data, it was observed that XRD spectra of Co-NiWO<sub>4</sub> represented the maximum of Miller indices values from NiWO<sub>4</sub>, except (002) and (310), which belong to the hkl planes associated with CoWO4 (JCPDS No. 15-0867). The obtained values of Miller indices suggested that the synthesized material is a solid solution instead of the mixture of CoWO<sub>4</sub> and NiWO<sub>4</sub>, implying that Co<sup>2+</sup> ions have successfully taken the lattice position in NiWO<sub>4</sub> due to the closeness of ionic radii of both Co<sup>2+</sup> and Ni<sup>2+</sup> ions [42]. The XRD spectra of Co-NiWO<sub>4</sub> NPs were composed of sharp peaks suggesting a crystalline nature with a wolframite monoclinic phase [50]. Further, the crystallite size and interplanar distance of Co-NiWO<sub>4</sub> were determined by the Scherer equation given by the following equations [51]:

$$D = \frac{0.9\lambda}{\beta \cos \theta},\tag{2}$$

Interlayer Spacing 
$$(d_{111}) = \frac{n\lambda}{2\sin\theta}$$
, (3)

where D is the size of the crystal,  $\lambda$  is the wavelength used (i.e., 1.5 Å),  $\beta$  is the half-width of the intense peak, and  $\theta$  is the diffraction angle. Using the XRD data in equation (2), the average crystallite size (D) was found to be 22 ± 0.05 nm with the interplanar distance  $d_{111}$  = 0.21 Å, which is found to be lesser than reported in the literature.

The morphology and topography of NiWO<sub>4</sub> and Co-NiWO<sub>4</sub> NPs were investigated using scanning electron microscopy (SEM) and their images are displayed in Figure 3(a) and (b). The pristine NiWO<sub>4</sub> (Figure 3a) appeared as a porous aggregation of small particles while Co-NiWO<sub>4</sub> NPs also appeared porous with the corrugated surface with some flakes with voids (Figure 3b). Therefore, SEM results supported the Co doping in the NiWO4, which was further verified by elemental composition analysis using EDX (Figure 3(c) and (d)). The EDX spectra of NiWO<sub>4</sub> in Figure 3(c) revealed the elemental composition as O (70.03%), Ni (14.75%), and W (15.22%); while the EDX spectra of Co-NiWO<sub>4</sub> NPs (Figure 3d) have the elemental composition as O (74.63%), Co (4.09%), Ni (5.88%), and W (15.40%). The EDX results revealed the presence of elements in stoichiometry and purity of the pristine and doped material. The uniformity of elemental distribution in the solid lattice was checked by elemental mapping analysis given in Figure S1, which suggests that all the elements are uniformly distributed over a range of space selected by the SEM image.

Further information about the shape and distribution of particles in the nanocomposite material upon doping of Co was assessed by TEM analysis, and the results are given

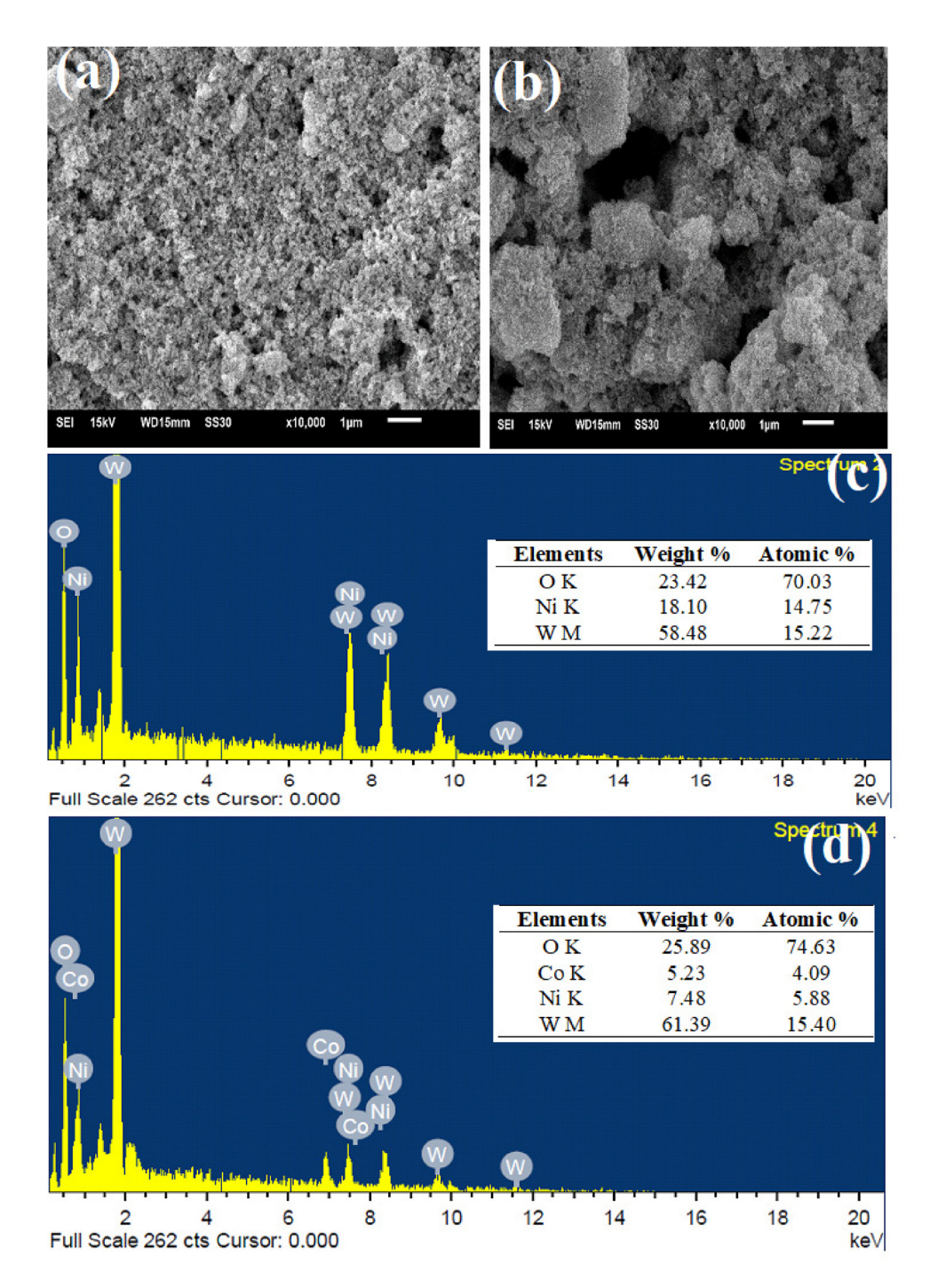


Figure 3: SEM-EDX image of (a, c) NiWO<sub>4</sub> and (b, d) Co-NiWO<sub>4</sub> NPs.

in Figure 4(a) and (b). Figure 4(a) represents the TEM image of Co–NiWO $_4$  NPs at 100 nm magnification bar showing the distribution of nanorods of size 24  $\pm$  0.35 nm. Further magnification at 20 nm bar TEM image ( Figure 4(b)) suggested a mitigated hexagonal type of geometry of the particles. The obtained value of particle size by TEM analysis is also approximately close to the Scherrer crystallite size.

The change in optical properties of the material upon Co doping was investigated by UV–Vis spectroscopy and the results are given in Figure 5(a). The UV–Vis profile of NiWO $_4$  (black line) has been given in the range of 200–600 nm and the presence of a small peak at 268 nm suggested the material to be UV light active. The type of transition could be attributed to the excitation of electrons from W and O within the WO $_6$ 

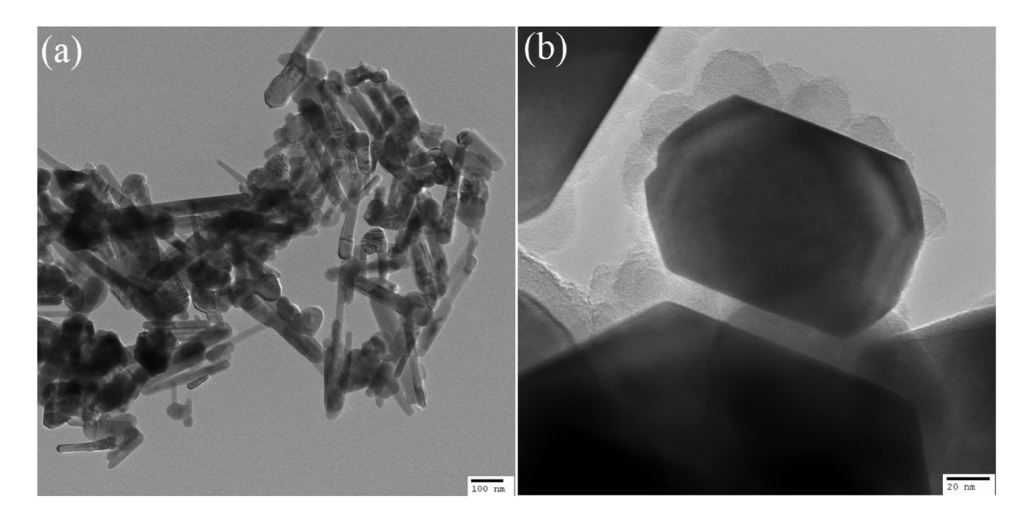


Figure 4: TEM images of Co-NiWO<sub>4</sub> NC: (a) 100 nm and (b) 20 nm magnification range.

matrix [51]. The UV-Vis spectra of  $CoWO_4$  given in Figure 5(a) (red line) exhibited a low-intensity broad spectrum at 588 nm, suggesting the material is visible light active. The UV spectra of  $Co-NiWO_4$  NPs exhibited two broad spectra, one in the range from 200 to 600 nm with absorption maxima at 354 nm and another at 667 nm with a low intensity suggesting the material to be both UV and visible light active. These bands could be attributed to the electron transition from  $^3A_{2g}$  to  $^1E_g$  and  $^3A_{2g}$  to  $^1T_{2g}$ , respectively, in the  $Ni^{2+}$   $O_6$  matrix [52]. The change in optical properties after doping of Co and the appearance of a broad spectrum is a direct reflectance of contribution from the Co-W metal charge transfer and Co-W metal charge transfer and Co-W and Co-W metal charge transfer and Co-W value of the pristine and doped material was calculated by the following equation [55]:

$$(\alpha h \nu) = A(h \nu - E_g)^n, \tag{4}$$

where h is the Planck constant,  $\alpha$  is the absorption coefficient, A is a constant,  $\nu$  is the frequency of radiation, and n is the constant of transition variation corresponding to n=2 as indirect transitions and n=1/2 belonging to direct transitions. The energy band gap value was obtained by extrapolating the linear part of the curve which cut the  $h\nu$  (eV) axis as illustrated in Figure 5(b). The values of  $E_g$  from Tauc's plot were obtained as 3.54 eV for NiWO<sub>4</sub>, 3.05 eV for CoWO<sub>4</sub>, and 1.58 eV for Co–NiWO<sub>4</sub> NC. From the literature, the band gap values of NiWO<sub>4</sub> have been reported as 2.53, 3.7, and 3.6 eV depending upon the synthesis protocols [43,56]. Therefore, the calculated value in the present study is in good agreement with the reported values. The

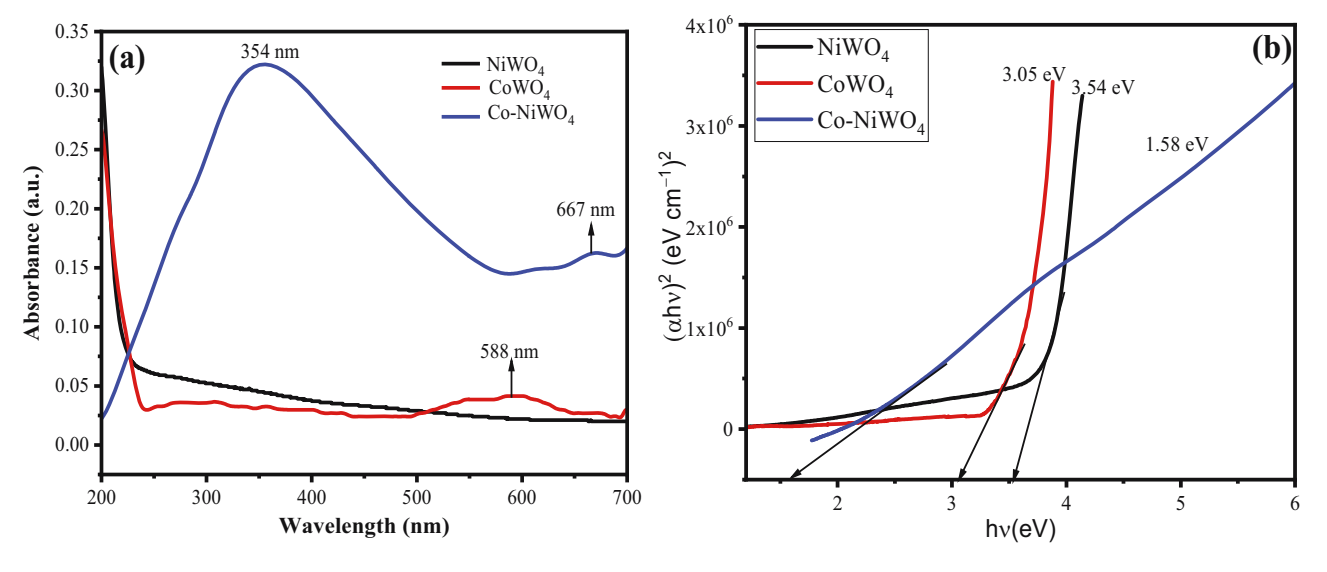


Figure 5: (a) UV-Vis spectra and (b) Tauc's plot for energy band gap for NiWO<sub>4</sub>, CoWO<sub>4</sub>, and Co-NiWO<sub>4</sub> NPs.

outcomes suggested that the Co doping in NiWO<sub>4</sub> created intermediate impurity level formation inside the band gap structure of NiWO<sub>4</sub>, which reduced its band gap and turned it into a promising catalyst for photocatalytic applications in visible light [57]. The UV–Vis analysis suggested that the optical properties of NiWO<sub>4</sub> can be tuned by Co doping, which results in greater light absorption capacity due to low band gap values.

Thermogravimetric analysis (TGA) was carried out to evaluate the thermal stability of the synthesized material Co–NiWO<sub>4</sub> NPs. Figure 6 shows the TGA profiles for NiWO<sub>4</sub>, CoWO<sub>4</sub>, and Co–NiWO<sub>4</sub>. The initial weight loss at a temperature of 200°C is due to the loss of water molecules and adsorbed gases. Further weight loss in the temperature range between 248.63 and 489.86°C is due to the loss of metal hydroxides or breakage in M–O linkages. The final weight loss beyond 490°C is due to the formation of intermediate products [58,59]. NiWO<sub>4</sub> shows a total weight loss of 43.28%, CoWO<sub>4</sub> shows 44.23%, and Co–NiWO<sub>4</sub> shows 45.69%.

# 3.2 Photocatalytic applications

#### 3.2.1 Selectivity test

To evaluate the photocatalytic efficiency of pristine  $NiWO_4$  and synthesized  $Co-NiWO_4$  NC, experiments were conducted using 10 mg of the catalyst with 10 mL of 50 ppm organic pollutant solution such as bromophenol (BP), methyl orange (MO), CR, malachite green (MG), crystal violet (CV), and methylene blue (MB) under visible solar radiation.

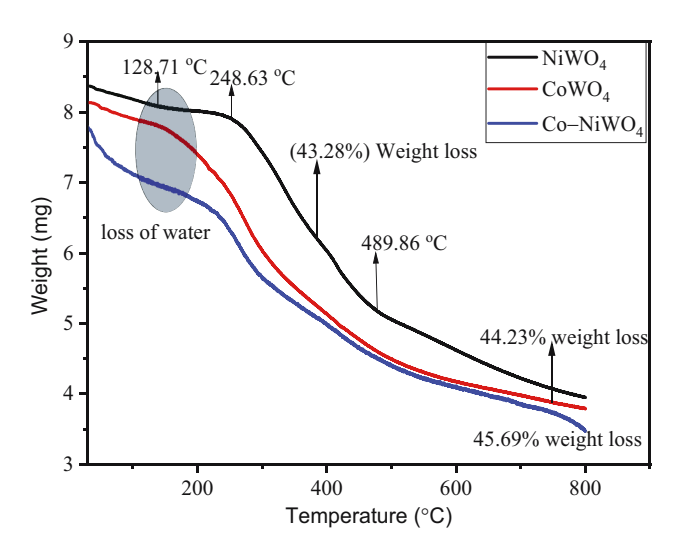


Figure 6: Thermogram profiles for NiWO $_4$  (black line), CoWO $_4$  (red line), and Co–NiWO $_4$  (blue line).

From the results shown in Figure S2(a–c), it was found that the synthesized material was most effective toward the degradation of the CR dye (88.20%) as compared to pristine NiWO<sub>4</sub> (38.13%) under the given conditions as compared to other organic pollutants. Therefore, Co doping in NiWO<sub>4</sub> has tuned the photocatalytic activity of Co–NiWO<sub>4</sub> NPs toward the CR dye. Hence, further photocatalytic experiments were designed for CR degradation by Co–NiWO<sub>4</sub> NC such as the effect of irradiation time, pH of the media, catalyst dose, and kinetics of the photocatalytic reaction with the mechanism.

#### 3.2.2 Effect of dye concentration and irradiation time

Figure 7(a-c) represents the UV-Vis spectra having variation of CR concerning irradiation time. With an increase in the irradiation time from 5 to 90 min, the absorbance values of the dye decrease indicating an increase in the photocatalytic degradation of the dye. A similar effect was observed with various dye concentrations of 30, 50, and 70 ppm having photocatalytic efficiencies of 91.45, 95.72, and 89.35% (Figure 7d). As can be seen, increasing the dye concentration from 30 to 50 ppm results in an increase in the photocatalytic efficiency from 91.45 to 95.72%, and with 70 ppm, it decreases to 89.35% [60]. Therefore, 50 ppm CR concentration was chosen as the optimized concentration for further photocatalytic experiments. The decrease in photocatalytic efficiency at high pollutant concentrations is due to the formation of an active layer of dye molecules above the surface of the catalyst acting as a screen. This screening effect hinders the path of light toward the surface of the catalyst and thus inhibits the generation of reactive oxidant species (ROS) such as 'OH or  ${}^{\bullet}O_2^{-}$  radicals to degrade the dye molecule [61].

#### 3.2.3 Effect of catalyst dose

The amount of catalyst to be utilized during the photocatalytic reaction is a very important factor in verifying the efficiency of the synthesized material. Photocatalytic experiments were carried out using 50 ppm CR concentration with 5, 10, 15, and 20 mg of Co–NiWO<sub>4</sub> NPs under visible radiations. The results obtained are shown in Figure 8(a and b), suggesting the 10 mg catalyst dose is optimal and exhibits a maximum photocatalytic efficiency of 91.81% under the given experimental conditions. Initially, as the catalyst dose increases from 5 to 10 mg, the photocatalytic efficiency increases from 77.81 to 91.81% due to a drastic increase in the number of active sites on the surface of the catalyst accommodating a greater number of dye molecules. As the

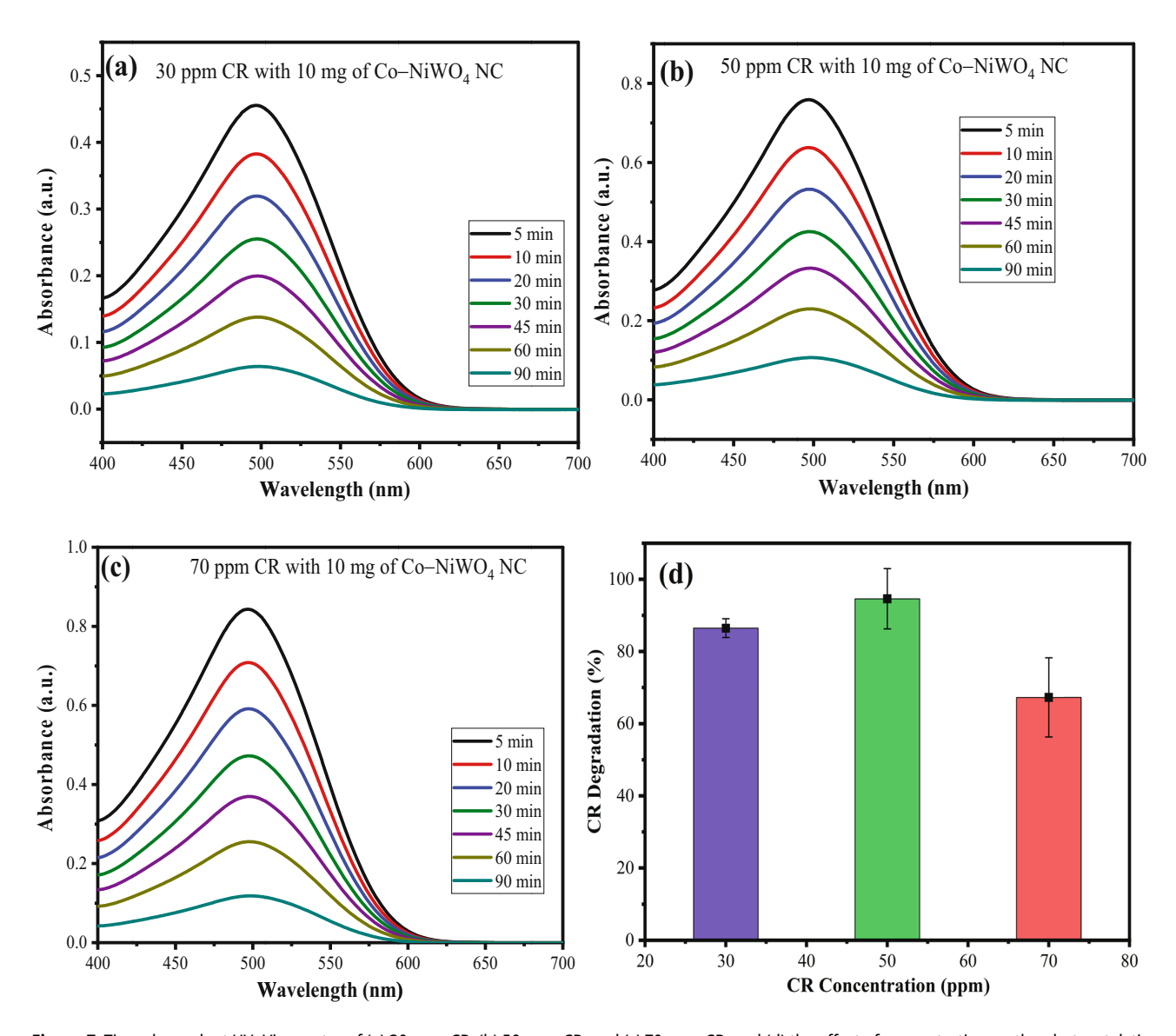


**Figure 7:** Time-dependent UV–Vis spectra of (a) 30 ppm CR, (b) 50 ppm CR, and (c) 70 ppm CR, and (d) the effect of concentration on the photocatalytic activity of Co–NiWO<sub>4</sub> NPs.

catalyst dose increases from 10 to 20 mg, the degree of agglomeration also increases, which reduces the number of surface-active sites of the catalyst, thereby lowering the photocatalytic efficiency observed [62].

#### 3.2.4 Effect of pH

The pH of the solution plays an important role in the degradation of dyes on the surface of the catalyst. To evaluate the optimized value of pH at which maximum photocatalytic activity can be achieved, experiments were performed by varying the solution pH from 2 to 8 under optimized reaction conditions. The results obtained are shown in

Figure 9(a) and (b), which suggests that maximum photocatalytic efficiency was achieved at pH 4 associated with 96.25% of CR degradation. Further increase in the pH value beyond 4 results in a decrease in photocatalytic efficiency. The trend can be explained based on the point of zero charges (pHpzc), which is equal to 5.4 as shown in Figure S3. At pH < 5.4, the surface of the catalyst is positive and susceptible to the negatively charged CR molecules *via* electrostatic forces of attraction, and thereby under the radiation degrades them using 'OH radicals. At pH > 5.4, the surface of the catalyst is negative, which would exert a negative repulsive force between the negatively charged CR molecules and the surface of the catalyst. So, fewer molecules of CR will adhere on the surface of the catalyst,

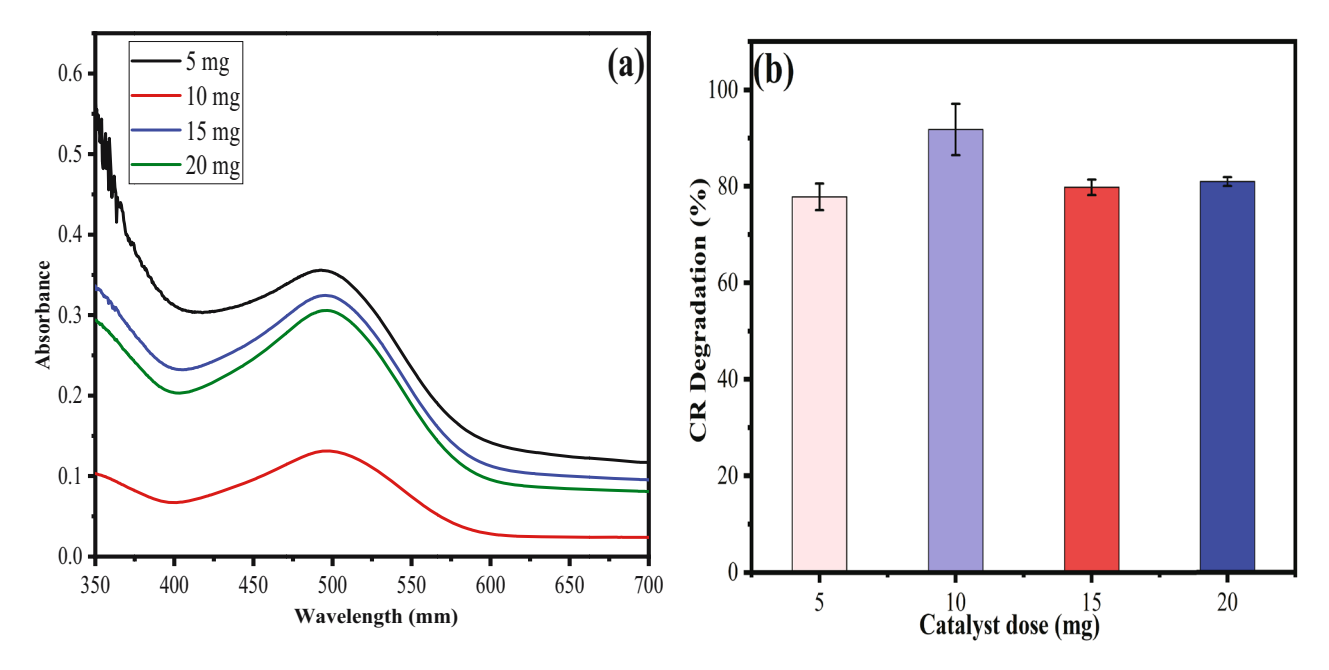


Figure 8: (a) UV–Vis absorption spectra for the effect of variable catalyst doses on CR degradation, and (b) bar graph representing the % CR degradation vs catalyst dose (mq).

and thereby a lower value of photocatalytic efficiency is obtained [63]. Hence, pH 4 was chosen as the optimized pH for further photocatalytic experiments.

#### 3.2.5 Effect of temperature

Photocatalytic experiments were conducted at temperatures from 298 to 328 K under the optimized reaction

conditions. The results obtained are shown in Figure 10(a and b), which suggests that an increase in the temperature of the system from 298 to 328 K reflects the increase in photocatalytic efficiency of Co–NiWO<sub>4</sub> NC to 86.63, 90.38, 93.14%, and finally 94.31%. The trend can be explained based on the fact that as the temperature increases, molecules gain more thermal energy, which results in greater collision frequency at high temperatures between the CR molecules and the surface of the catalyst. Moreover, the

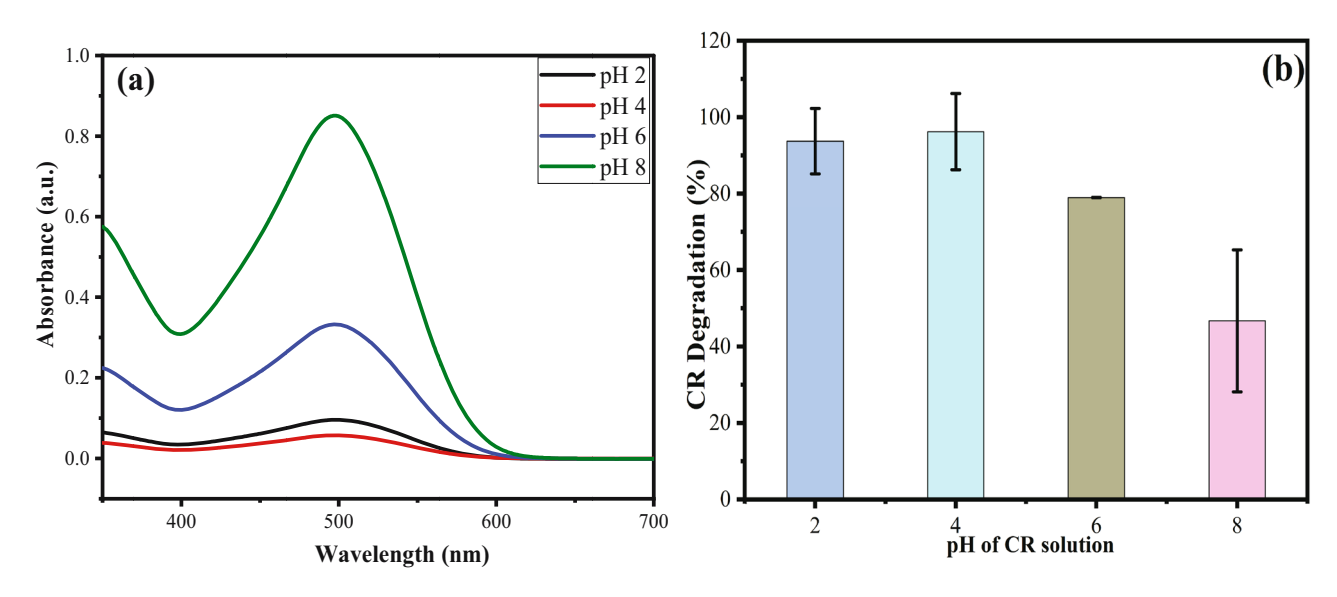
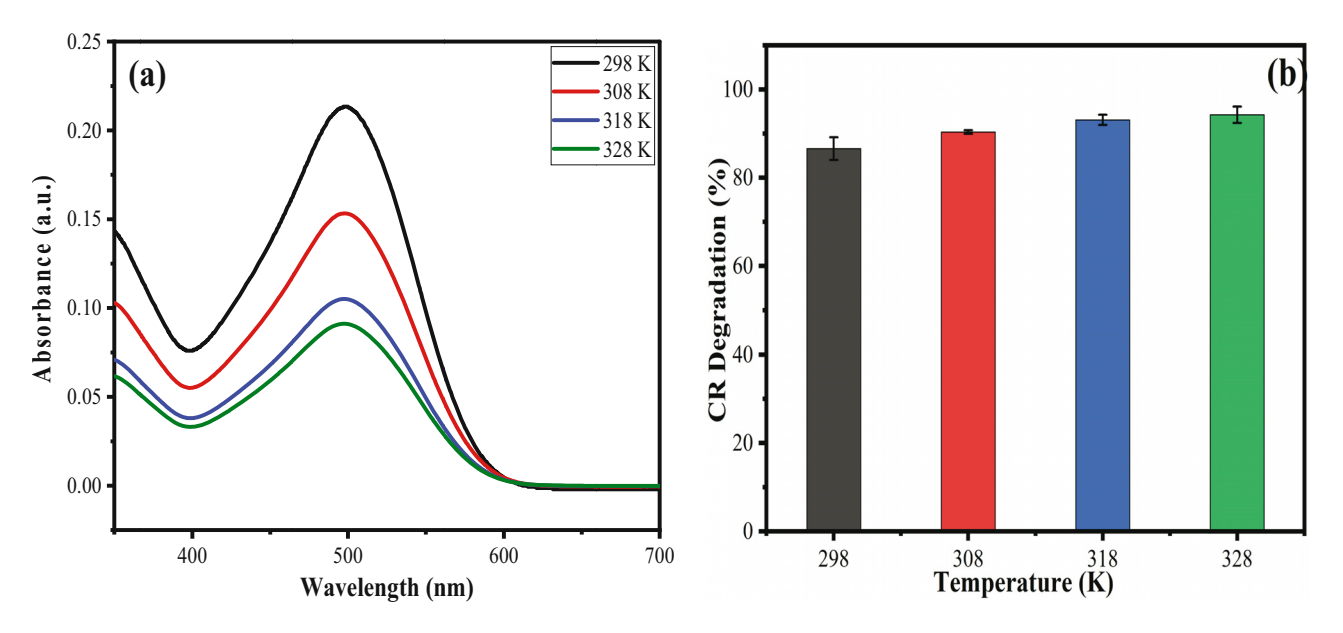


Figure 9: (a) UV–Vis absorption spectra for the effect of various pH on CR degradation, and (b) bar graph representing the % CR degradation vs pH of the medium.



**Figure 10:** (a) UV–Vis absorption spectra for the effect of various temperatures (298–329 K) on CR degradation, and (b) bar graph representing the % CR degradation *vs* temperature.

molecules can gain sufficient energy, which enables them to cross the activation energy barrier and thus high photocatalytic activity is obtained [64].

#### 3.2.6 Effect of visible light intensity

The intensity of the radiation source ( $\lambda > 420$  nm) greatly influences the decolorization reaction, and to observe this photocatalytic experiments were performed under the optimized reaction conditions for various light intensities

such as 26.4, 45.5, 78.3, and 92.5 mW cm<sup>-2</sup>. The results obtained are shown in Figure 11(a and b). It can be seen from the results that as the light intensity increases, the photocatalytic efficiency of the synthesized material also increases achieving an optimized value of 95.29% CR degradation at 92.5 mW cm<sup>-2</sup>. The trend can be explained based on the fact that an increase in light intensity causes an increase of more amount of light on the catalyst surface and thus a high rate of photoabsorption, which produces a greater number of hydroxyl radicals resulting in high photocatalytic activity [65].

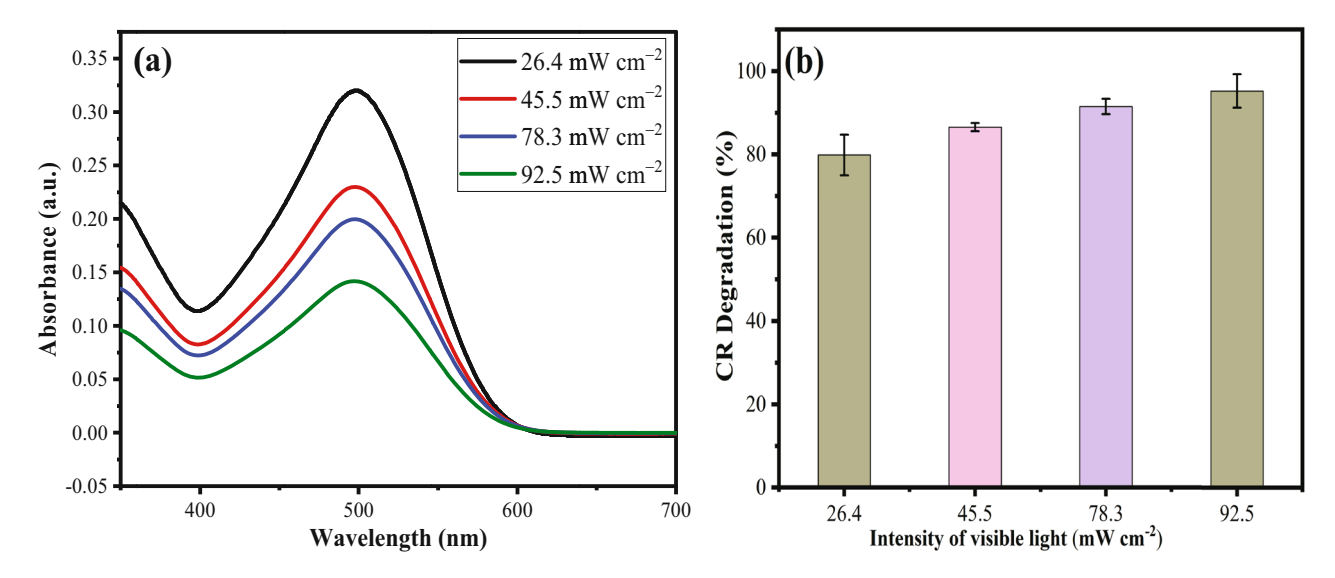


**Figure 11:** (a) UV–Vis absorption spectra for the effect of various visible light power intensities on CR degradation, and (b) bar graph representing the % CR degradation *vs* power intensity.

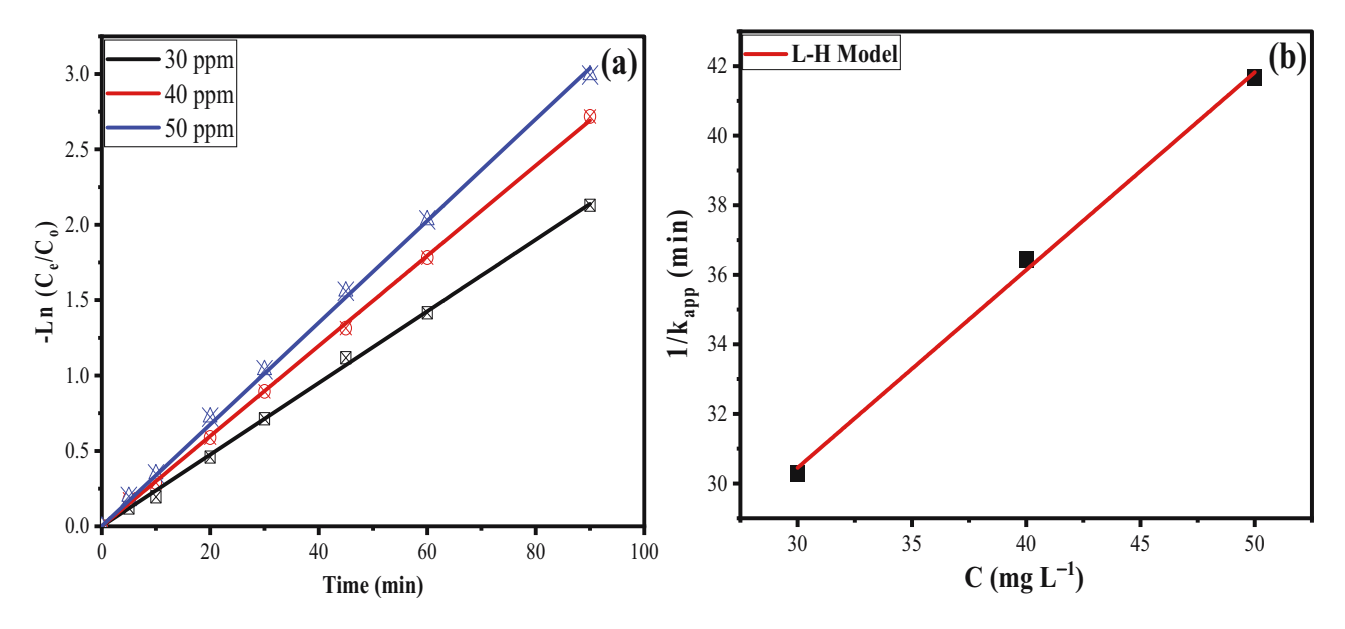


Figure 12: (a)  $-\ln(C_e/C_0)$  versus irradiation time for all studied concentrations of the CR plot. (b) L-H plot for  $(1/k_{app})$  versus CR concentration.

## 3.3 Kinetics of the reaction

The kinetic data obtained from photocatalytic experiments were adjusted to L–H first-order kinetic model, as given by the following equations [66,67]:

$$-\ln\left(\frac{C_{\rm e}}{C_0}\right) = k_{\rm app} \times t,\tag{5}$$

$$V = k_{\rm app} \times C = \frac{k_r k_s C}{1 + k_s C},\tag{6}$$

$$\frac{1}{k_{\rm app}} = \frac{1}{k_{\rm r}k_{\rm s}} + \frac{C}{k_{\rm r}},\tag{7}$$

where  $C_0$  and  $C_e$  are the concentrations of CR at the initial state (t=0) and each time interval,  $k_{\rm app}$  is the rate constant,  $k_{\rm s}$  (L/mg) is the adsorption constant, and  $k_{\rm r}$  (mg/L min) is the reaction rate. Figure 12(a) represents a plot of  $-\ln(C_e/C_0)$  versus irradiation time for all studied concentrations of CR, which gives the apparent constant ( $k_{\rm app}$ ) values as listed in Table 1 with correlation coefficients ( $R^2$ ). The value of  $k_{\rm app}$  (0.034 min<sup>-1</sup> for 30 ppm, 0.028 for 40 ppm, and 0.025 min<sup>-1</sup> for 50 ppm CR) decreases with an increase in the CR concentration. The value of photocatalytic half-life value ( $t_{\rm 1/2}=\ln 2/k_{\rm app}$ ) was evaluated as 20.38 min for 30 ppm, 24.75 min

for 40 ppm, and 27.72 min for 50 ppm CR concentration. The values of  $k_{\rm app}$  are very significant in correlating the characteristics of the photocatalytic reaction with the L–H model at low dye concentrations. Figure 12(b) represents the graph  $(1/k_{\rm app})$  versus CR concentration, which appears as linear, suggesting the validity of the L–H model with photocatalytic data of CR degradation. Using equation (7), the value of the adsorption constant  $(k_{\rm s})$  and the reaction rate  $(k_{\rm r})$  were found to be 0.42 L/mg and 0.76 mg/L min, respectively. The value of  $k_{\rm r}$  was found to be greater than the value of  $k_{\rm s}$  which suggests that photoabsorption is the rate-determining step, *i.e.*, the photocatalytic reaction starts with the absorption of light by the surface of the catalyst [68].

# 3.4 Scavenger experiment and mechanism of photodegradation

To evaluate the type of ROS involved in CR degradation, scavenger experiments were performed by taking 10 mg of Co–NiWO<sub>4</sub> NPs with 30 ppm of CR with 1.5 mmol each of isopropyl alcohol (IPA) for 'OH radical, benzoquinone (BQ) for 'O<sub>2</sub> radical, acrylamide (AA) for  $e_{CB}^-$ , and potassium iodide (KI) for  $h_{vb}^+$  under visible solar radiation for 90 min [56,69]. The

Table 1: L-H first-order kinetic parameters for photocatalytic degradation of CR by Co-NiWO<sub>4</sub> NPs

CR concentration (ppm)	$k_{app}$	Error	t <sub>1/2</sub>	R <sup>2</sup>	<b>k</b> <sub>r</sub>	k <sub>s</sub>
30	0.034	$2.07 \times 10^{-4}$	20.98	0.999	0.76	0.42
40	0.028	$1.66 \times 10^{-4}$	24.75	0.999		
50	0.025	$2.66 \times 10^{-4}$	27.72	0.999		

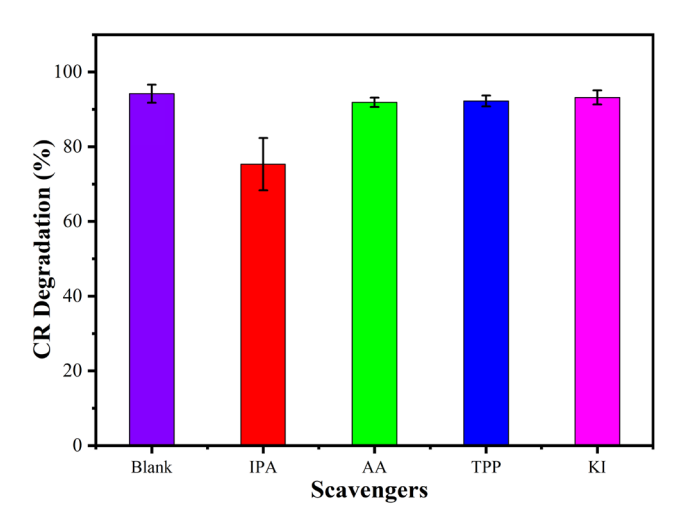


**Figure 13:** Effect of scavengers on the photocatalytic efficiency of Co–NiWO<sub>4</sub> NPs under optimized conditions.

obtained results after the reaction are shown in Figure 13 which suggested that it is 'OH radicals that act as primary ROS in CR degradation as, in the presence of IPA, maximum suppression of photocatalytic efficiency (63.34%) occurs.

The hypothetical reaction mechanism of CR degradation is given as [3–5] follows:

$$\begin{split} &\text{Co-NiWO}_4 + h\nu \rightarrow \text{Co-NiWO}_4(h_{VB}^+ + e_{CB}^-) \\ &\text{Co-NiWO}_4(h_{VB}^+) + \text{OH}_{ad}^- \rightarrow \text{OH} \\ &\text{Co-NiWO}_4(e_{CB}^-) + \text{O}_2 \rightarrow \text{O}_2^- \\ &\text{O}_2^- + \text{H}^+ \rightarrow \text{HO}_2 \\ &2\text{HO}_2 \rightarrow \text{O}_2 + \text{H}_2\text{O}_2 \\ &\text{H}_2\text{O}_2 + e_{CB}^- \rightarrow \text{OH} + \text{OH}^- \\ &\text{OH} + \text{CR}(\text{dye}) \xrightarrow{\text{OH}} \text{CO}_2 + \text{H}_2\text{O} \end{split}$$

As the solar radiation falls on the surface of the catalyst, the photoabsorption process occurs in which the excitation of an electron from the valence band (VB) to the conduction band (CB) occurs, thus creating a hole (h $^+$ ) in VB and photogenerated e $^-$  in CB. The holes interact with water molecules of the media and thus oxidize them to highly excited 'OH radicals. Similarly, photogenerated e $^-$  in CB interacts with the surface adsorbed oxygen on Co–NiWO<sub>4</sub> NPs and thus transforms them to highly reactive 'O $_2$  radicals, which further combine with protons (H $^+$  ions) to form 'OH $_2$  radicals. These 'OH $_2$  radicals further unite to form H $_2$ O $_2$ , which is further attacked by photogenerated e $^-$  and thus form 'OH radicals, which are responsible for the mineralization of CR [60,70].

# 3.5 Effect of leaching experiments

Various radiation processes such as photolysis (CR solution under radiation without catalyst), adsorption (CR solution with the catalyst in the dark), and CR solution with catalyst under UV and visible light were tested under optimized conditions. The results obtained are shown in Figure S4(a and b), which suggest that under visible light radiation CR is degraded to a maximum (94.96%). The effect of photolysis (2.13%) was negligible while adsorption plays a significant role by adsorbing 64.23% of the CR dye and UV light resulted in 86.19% of CR degradation. Therefore, for the best possible results, visible light as radiation was chosen for further photocatalytic experiments.

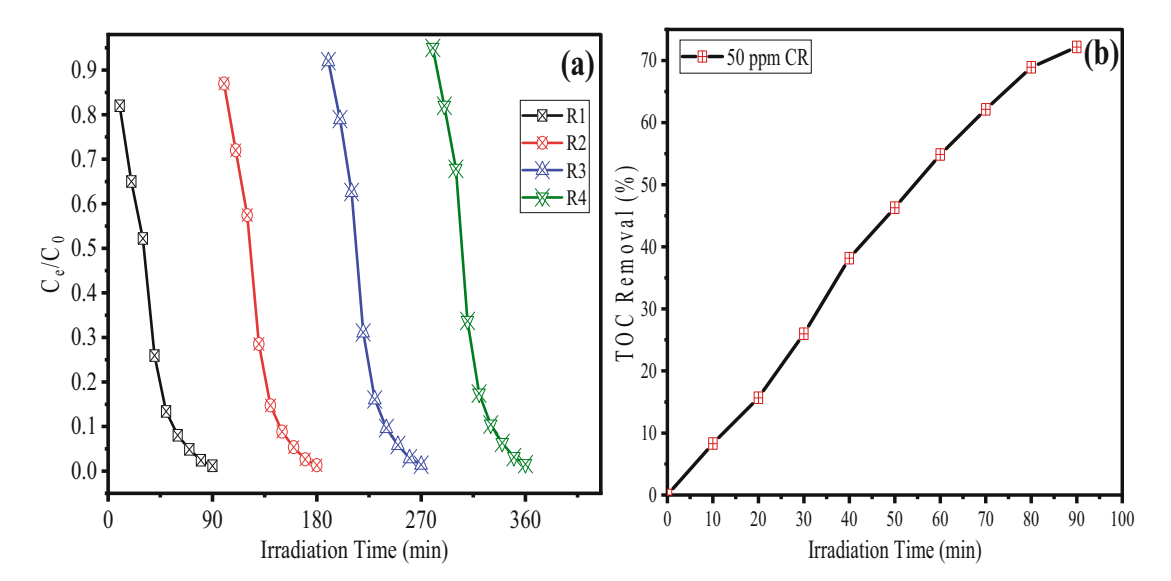


Figure 14: (a) Reusability test for the synthesized Co-NiWO<sub>4</sub> NPs. (b) TOC analysis during degradation of CR.

Table 2: Comparison with the literature

Materials	Light source used	Dye used	Irradiation time (min)	%CR degradation	Ref.
Ag/ZnO	UV light	CR	180	81.60	[61]
Graphene-TiO <sub>2</sub>	Sunlight	CR	60	90.00	[71]
MnFe2O4/TA/ZnO	Xenon lamp	CR	90	84.20	[72]
P-ZrO <sub>2</sub> CeO <sub>2</sub> ZnO	LED light	CR	250	85.85	[73]
Doped ZnO-Gd	Visible light	CR	120	68.02	[74]
CS-BiOCI/ZnO	UV light	CR	40	93	[75]
Co-NiWO <sub>4</sub>	Visible light	CR	90	95.00	Present study

## 3.6 Reusability and TOC test

The stability and reusability of the synthesized material are important aspects of experimental studies and to evaluate this, photocatalytic experiments were performed under optimized reaction conditions in a cyclic mode. In cycle 1, 10 mg of Co-NiWO<sub>4</sub> NPs was dispersed in 20 mL of 50 ppm CR solution at pH 4, a temperature of 328 K, visible light power intensity of 92.5 mW cm<sup>-2</sup> for 90 min. After the completion of the reaction, the material was separated by centrifugation and the supernatant was utilized under a UV-Vis spectrophotometer for the remaining concentration of CR after degradation. The collected material was washed with distilled water and ethanol and dried in a hot air oven at 50°C for 2 h. The material was again utilized for cycle 2 of CR degradation and regeneration. This procedure was repeated till four cycles of regeneration and the obtained results are shown in Figure 14(a), which suggests even after four consecutive cycles of reuse, the photocatalytic efficiency of the material decreased from 96 to 92%. The reusability experiments suggested that the synthesized material is highly stable toward photocatalytic degradation of CR dye.

The mineralization of CR by Co-NiWO<sub>4</sub> NPs was followed by total organic carbon (TOC) analysis using a TOC analyzer (Matelar Toledo). The results obtained are shown in Figure 14(b), which suggest that as the irradiation time increases, the TOC removal (%) increases continuously and finally the material achieves a total of 72% TOC removal. The TOC (%) was calculated using the following equation:

$$TOC (\%) = \left(\frac{TOC_0 - TOC_f}{TOC_0}\right) \times 100.$$
 (8)

# 3.7 Comparison with the literature

To check the add-on information concluded by the present study to the literature, the reaction conditions with maximum efficiency toward organic pollutants were compared and are given in Table 2.

## 4 Conclusion

The current study focuses on the hydrothermal synthesis of Co-doped NiWO<sub>4</sub> NPs at 180°C, utilizing a Teflon-lined autoclave. The results revealed significant morphological, crystallographic, and spectroscopic changes induced by Co doping in the nanocrystalline solid. The XRD spectra of Co-NiWO<sub>4</sub> NPs displayed sharp peaks, indicating a crystalline nature with a wolframite monoclinic phase. The UV spectra of Co-NiWO<sub>4</sub> NPs exhibited two broad bands at 354 and 667 nm, suggesting that the material is active in both UV and visible light regions. EDX analysis confirmed the presence of elements in stoichiometric proportions, ensuring the purity of the pristine and doped materials. The synergistic effect of dopants led to alterations in various parameters such as d spacing, atomic positions, orientations, average crystallite size, surface morphology, and thermal stability. Notably, the energy band gap reduced from 3.75 (for NiWO<sub>4</sub>) to 1.75 eV in Co-NiWO<sub>4</sub> NPs, resulting in enhanced photocatalytic activity toward CR degradation. The photocatalytic efficiency increased from 38.13% with pristine NiWO<sub>4</sub> to an impressive 88.20% with Co-NiWO<sub>4</sub> NPs, reaching 95% after optimizing the reaction conditions. The optimized parameters included 50 ppm CR concentration, 10 mg catalyst dose, pH 4, an irradiation time of 90 min, a temperature of 328 K, and a light intensity of 92.5 mW cm $^{-2}$ . The photocatalytic data fit well with the L-H pseudo-first-order model, with  $k_{\rm app}$  values of 0.034 min<sup>-1</sup> for 30 ppm, 0.028 min<sup>-1</sup> for 40 ppm, and 0.025 min<sup>-1</sup> for 50 ppm CR, displaying a correlation coefficient of 0.99. Trapping experiments revealed that 'OH radicals primarily acted as ROS in CR degradation. Moreover, reusability experiments demonstrated the high stability of the synthesized Co-NiWO<sub>4</sub> NPs for photocatalytic CR degradation. The findings strongly support the outstanding efficiency of Co-NiWO<sub>4</sub> NPs in treating organic

pollutants in wastewater. As prospects, we intend to explore the photocatalytic water splitting and hydrogen production potential of these multi-metal tungstate NPs.

**Acknowledgments:** The authors extend their thanks to Researchers Supporting Project (Ref: RSPD2023R670), King Saud University, Riyadh, Saudi Arabia.

**Funding information:** This research was funded by The Researchers Supporting Project (Ref: RSPD2023R670), King Saud University, Riyadh, Saudi Arabia.

**Author contributions:** All authors have accepted responsibility for the entire content of this manuscript and approved its submission.

**Conflict of interest:** The authors state no conflict of interest.

**Data availability statement:** The data that support the findings of this study are available on reasonable request from the corresponding author.

# References

- [1] Vattikuti SVP, Byon C, Ngo IL. Highly crystalline multi-layered WO3 Sheets for photodegradation of congo red under visible light irradiation. Mater Res Bull. 2016;84:288–97. doi: 10.1016/J. MATERRESBULL.2016.08.008.
- [2] Mayoufi A, Nsib MF, Houas A. Doping level effect on visible-light irradiation W-Doped TiO2–anatase photocatalysts for congo red photodegradation. Comptes Rendus Chimie. 2014;17:818–23. doi: 10.1016/I.CRCI.2014.01.019.
- [3] Wang W, Lu T, Chen Y, Tian G, Sharma VK, Zhu Y, et al. Mesoporous silicate/carbon composites derived from dye-loaded palygorskite clay waste for efficient removal of organic contaminants. Sci Total Environ. 2019;696:133955.
- [4] Wang Y, Pan Y, Zhu T, Wang A, Lu Y, Lv L, et al. enhanced performance and microbial community analysis of bioelectrochemical system integrated with bio-contact oxidation reactor for treatment of wastewater containing azo dye. Sci Total Environ. 2018:634:616–27.
- [5] Guo K, Gao B, Tian X, Yue Q, Zhang P, Shen X, et al. Synthesis of Polyaluminium Chloride/Papermaking Sludge-Based Organic Polymer Composites for Removal of Disperse Yellow and Reactive Blue by Flocculation. Chemosphere. 2019;231:337–48.
- [6] Amanulla B, Sannasi S, Abubakar AKM, Ramaraj SK. A Magnetically Recoverable Bimetallic Au-FeNPs Decorated on g-C3N4 for Efficient Photocatalytic Degradation of Organic Contaminants. J Mol Liq. 2018;249:754–63.
- [7] Nasirian M, Mehrvar M. Photocatalytic degradation of aqueous methyl orange using nitrogen-doped TiO2 photocatalyst prepared by novel method of ultraviolet-assisted thermal synthesis. J Environ Sci. 2018;66:81–93.

- [8] Aziz A, Ali N, Khan A, Bilal M, Malik S, Ali N, et al. Chitosan-zinc sulfide nanoparticles, characterization and their photocatalytic degradation efficiency for Azo Dyes. Int J Biol Macromol. 2020;153:502–12.
- [9] Aboutaleb WA, El-Salamony RA. Effect of Fe2O3-CeO2 nanocomposite synthesis method on the congo red dye photodegradation under visible light irradiation. Mater Chem Phys. 2019;236:121724. doi: 10.1016/J.MATCHEMPHYS.2019.121724.
- [10] Boudiaf S, Nasrallah N, Mellal M, Belhamdi B, Belabed C, Djilali MA, et al. Kinetic studies of congo red photodegradation on the hetero-system CoAl2O4/ZnO with a stirred reactor under solar light. J Environ Chem Eng. 2021;9:105572. doi: 10.1016/j.jece.2021. 105572.
- [11] Said M, Rizki WT, Asri WR, Desnelli D, Rachmat A, Hariani PL. SnO2–Fe3O4 nanocomposites for the photodegradation of the congo red dye. Heliyon. 2022;8:e09204. doi: 10.1016/j.heliyon.2022. e09204.
- [12] Hao M, Meng X, Miao Y. Synthesis of NiWO 4 powder crystals of polyhedron for photocatalytic degradation of rhodamine. Solid State Sci. 2017;72:103–8. doi: 10.1016/j.solidstatesciences.2017. 08.018.
- [13] Shee NK, Kim H-J. Sn(IV) porphyrin-based ionic self-assembled nanostructures and their application in visible light photo-degradation of malachite green. Catalysts. 2022;12:799. doi: 10.3390/ catal12070799.
- [14] Idriss H, Ibrahem MA, Modwi A. Photocatalytic degradation of congo red pigment by V2O5-TiO2nanohybrid. Z Naturforschung -Sect A J Phys Sci. 2023;78(1):67–76.
- [15] Jamal N, Radhakrishnan A, Raghavan R, Bhaskaran B. Efficient photocatalytic degradation of organic dye from aqueous solutions over zinc oxide incorporated nanocellulose under visible light irradiation. Main Group Met Chem. 2020;43(1):84–91.
- [16] Kora AJ. Gum tragacanth-mediated synthesis of metal nanoparticles, characterization, and their applications as a bactericide, catalyst, antioxidant, and peroxidase mimic. Green Process Synth. 2023;12(1):20228138.
- [17] Khan Y, Sharafat U, Gul S, Khan MI, Ismail M, Khan MA, et al. Novel in situ synthesis of quaternary core–shell metallic sulfide nanocomposites for degradation of organic dyes and hydrogen production. Green Process Synth. 2023;12(1):20228128.
- [18] Pouretedal HR, Narimany S, Keshavarza MH. Nanoparticles of ZnS Doped with Iron as Photocatalyst under UV and Sunlight Irradiation. Int J Mater Res. 2010;101(8):1046–51.
- [19] Nisar J, Hassan S, Khan MI, Iqbal M, Nazir A, Sharif A, et al. Hetero-Structured Iron Molybdate Nanoparticles: Synthesis, Characterization and Photocatalytic Application. Int J Chem React Eng. 2020;18(2):20190123.
- [20] Aravinthkumar K, Praveen E, Jacquline Regina Mary A, Raja Mohan C. Investigation on SrTiO3 Nanoparticles as a Photocatalyst for Enhanced Photocatalytic Activity and Photovoltaic Applications. Inorg Chem Commun. 2022;140:109451. doi: 10.1016/J.INOCHE. 2022.109451.
- [21] Puga F, Navío JA, Hidalgo MC. Boosting the Photocatalytic Properties of NaTaO3 by Coupling with AgBr. Photochem Photobiol Sci. 2022;22(3):549–66. doi: 10.1007/S43630-022-00334-9/ TABLES/3.
- [22] Anzai A, Yamamoto A, Yoshida H. BaTi4O9 Photocatalysts with Variously Loaded Ag Cocatalyst for Highly Selective Photocatalytic CO2 Reduction with Water. Catal Lett. 2022;152(8):2498–506. doi: 10.1007/S10562-021-03831-1/METRICS.

- [23] Zhang Y, Selvaraj R, Sillanpää M, Kim Y, Tai CW. Coprecipitates Synthesis of CaIn2O4 and Its Photocatalytic Degradation of Methylene Blue by Visible Light Irradiation. Ind Eng Chem Res. 2014;53(29):11720–6. doi: 10.1021/IE403401Y.
- [24] Abbas S, Bibi I, Majid F, Ata S, Ibrahim SM, Kamal S, et al. Microemulsion synthesis of La1-XCrxFeO3nanoparticles: Effect of Cr doping on ferroelectric, dielectric and photocatalytic properties. Int J Chem React Eng. 2020;18(10–11):20190201. doi: 10.1515/IJCRE-2019-0201/ASSET/GRAPHIC/J\_IJCRE-2019-0201\_FIG\_013.JPG.
- [25] Thanh Truc NT, Pham TD, Van Thuan D, Son LT, Tran DT, Nguyen MV, et al. Superior activity of Cu-NiWO4/g-C3N4 Z direct system for photocatalytic decomposition of VOCs in aerosol under visible light. J Alloy Compd. 2019;798:12–8.
- [26] Mousavi M, Habibi-Yangjeh A. Decoration of Fe3O4 and CoWO4 nanoparticles over graphitic carbon nitride: Novel visible-lightresponsive photocatalysts with exceptional photocatalytic performances. Mater Res Bull. 2018;105:159–71.
- [27] Mohamed Jaffer Sadiq M, Krishna Bhat D. Novel NiWO4-ZnO-NRGO ternary nanocomposites with enhanced photocatalytic activity. Mater Today Proc. 2018;5:22412–20. doi: 10.1016/j.matpr.2018. 06.610.
- [28] Lakshmi Prabavathi S, Muthuraj V. Superior visible light driven photocatalytic degradation of fluoroquinolone drug norfloxacin over novel NiWO4 nanorods anchored on G-C3N4 nanosheets. Colloids Surf A Physicochem Eng Asp. 2019;567:43–54. doi: 10.1016/ j.colsurfa.2019.01.040.
- [29] Liaquat H, Imran M, Latif S, Iqbal S, Hussain N, Bilal M. Citric acid-capped NiWO4/Bi2S3 and RGO-Doped NiWO4/Bi2S3 nanoarchitectures for photocatalytic decontamination of emerging pollutants from the aqueous environment. Environ Res. 2022;212:113276. doi: 10.1016/j.envres.2022.113276.
- [30] Habibi-Yangjeh A, Feizpoor S. Combination of NiWO4 and polyaniline with TiO2: fabrication of ternary photocatalysts with highly visible-light-induced photocatalytic performances. J Iran Chem Soc. 2020;17(2):351–65.
- [31] Kamaraj E, Lee YR, Balasubramani K. Fabrication of a visible-light-driven p-Type NiWO4/n-Type SnO2 heterojunction with efficient photocatalytic activity for degradation of amaranth. J Chin Chem Soc. 2022;69(7):1020–31. doi: 10.1002/ICCS.202200009.
- [32] Faka V, Griniezaki M, Kiriakidis G, Grilla E, Mantzavinos D, Mao S, et al. Solar light induced photocatalytic degradation of sulfamethoxazole by ZnWO4/CNNs nanocomposites. J Photochem Photobiol A Chem. 2022;432:114108. doi: 10.1016/j.jphotochem. 2022.114108.
- [33] Zhang C, Zhang H, Zhang K, Li X, Leng Q, Hu C. Photocatalytic Activity of ZnWO4: Band Structure, Morphology and Surface Modification. ACS Appl Mater Interfaces. 2014;6(16):14423–32. doi: 10.1021/AM503696B/ASSET/IMAGES/MEDIUM/AM-2014-03696B\_ 0008.GIF.
- [34] Faka V, Tsoumachidou S, Moschogiannaki M, Kiriakidis G, Poulios I, Binas V. ZnWO4 nanoparticles as efficient photocatalyst for degradation of para-aminobenzoic acid: impact of annealing temperature on photocatalytic performance. J Photochem Photobiol A Chem. 2021;406:113002. doi: 10.1016/J.JPHOTOCHEM. 2020.113002
- [35] Nie J, Hassan QU, Jia Y, Gao J, Peng J, Lu J, et al. La-Doped ZnWO4 Nanorods with Enhanced Photocatalytic Activity for NO Removal: Effects of La Doping and Oxygen Vacancies. Inorg Chem Front. 2020;7(2):356–68. doi: 10.1039/C9QI01152H.

- [36] Huang C, Chen L, Li H, Mu Y, Yang Z. Synthesis and Application of Bi2WO6 for the Photocatalytic Degradation of Two Typical Fluoroquinolones under Visible Light Irradiation. RSC Adv. 2019;9(48):27768–79. doi: 10.1039/C9RA04445K.
- [37] Saraf R, Shivakumara C, Behera S, Nagabhushana H, Dhananjaya N. Facile Synthesis of PbWO4: Applications in Photoluminescence and Photocatalytic Degradation of Organic Dyes under Visible Light. Spectrochim Acta A Mol Biomol Spectrosc. 2015;136(PB):348–55. doi: 10.1016/I.SAA.2014.09.038.
- [38] Tri NL, Duc DS, Van Thuan D, Al Tahtamouni T, Pham TD, Tran DT, et al. Superior Photocatalytic Activity of Cu Doped NiWO4 for Efficient Degradation of Benzene in Air Even under Visible Radiation. Chem Phys. 2019;525:110411. doi: 10.1016/j.chemphys. 2019.110411.
- [39] Chatterjee M, Saha S, Chatterjee T, Das S, Pradhan SK. Mn-Doped NiWO4 quantum dots with superior electrochemical and conductivity performance for energy storage application. J Energy Storage. 2022;56:105946. doi: 10.1016/j.est.2022.105946.
- [40] H H, John M, Jose A, Kuriakose S, Varghese T. Influence of Bi3 + Doping on Structural, Optical and Photocatalytic Degradation Properties of NiWO4 Nanocrystals. J Solid State Chem. 2021;295:121892. doi: 10.1016/j.jssc.2020.121892.
- [41] Flihh SM, Ammar SH. Fabrication and photocatalytic degradation activity of Core/Shell ZIF-67@CoWO4@CoS heterostructure photocatalysts under visible light. Env Nanotechnol Monit Manag. 2021;16:100595. doi: 10.1016/j.enmm.2021.100595.
- [42] Wahba MA, Yakout SM, Khaled R. Interface engineered efficient visible light photocatalytic activity of MWCNTs/Co doped ZnO nanocomposites: morphological, optical, electrical and magnetic properties. Opt Mater (Amst). 2021;115:111039. doi: 10.1016/j. optmat.2021.111039.
- [43] Alam U, Verma N. Direct Z-scheme-based novel cobalt nickel tungstate/graphitic carbon nitride composite: Enhanced photocatalytic degradation of organic pollutants and oxidation of benzyl alcohol. Colloids Surf A Physicochem Eng Asp. 2021;630:127606. doi: 10.1016/j.colsurfa.2021.127606.
- [44] Dridi R, Dridi D, Hammami S, Dimassi W, Chtourou R, Amlouk M. Growth and Physical Investigations on NiWO4 Thin Films as a Potential for NO2 Sensing. Opt (Stuttg). 2023;273:170330. doi: 10. 1016/J.IJLEO.2022.170330.
- [45] Niu L, Li Z, Xu Y, Sun J, Hong W, Liu X, et al. Simple Synthesis of Amorphous NiWO4 Nanostructure and Its Application as a Novel Cathode Material for Asymmetric Supercapacitors. ACS Appl Mater Interfaces. 2013;5(16):8044–52. doi: 10.1021/AM402127U/SUPPL\_ FILE/AM402127U\_SI\_001.PDF.
- [46] Mani S, Vediyappan V, Chen SM, Madhu R, Pitchaimani V, Chang JY, et al. Hydrothermal synthesis of NiWO4 crystals for high performance non-enzymatic glucose biosensors. Sci Rep. 2016;6(1):1–8. doi: 10.1038/srep24128.
- [47] Oliveira YL, Costa MJS, Jucá ACS, Silva LKR, Longo E, Arul NS, Cavalcante LS. Structural characterization, morphology, optical and colorimetric properties of NiWO4 crystals synthesized by the coprecipitation and polymeric precursor methods. J Mol Struct. 2020;1221:128774. doi: 10.1016/J.MOLSTRUC.2020.128774.
- [48] Rosal FJO, Gouveia AF, Sczancoski JC, Lemos PS, Longo E, Zhang B, et al. Electronic structure, growth mechanism, and sonophotocatalytic properties of sphere-like self-assembled NiWO4 nanocrystals. Inorg Chem Commun. 2018;98:34–40. doi: 10.1016/j.inoche. 2018.10.001.

- [49] Abdul Kader HD, Sh. Mohammed I, Ammar SH. Synthesis of recyclable core/shell CoFe2O4@CoWO4 photocatalysts for efficient visible-light photocatalytic degradation of environmental pollutants. Environ Nanotechnol Monit Manag. 2022;17:100664. doi: 10. 1016/j.enmm.2022.100664.
- [50] Karthiga R, Kavitha B, Rajarajan M, Suganthi A. Photocatalytic and antimicrobial activity of NiWO4 nanoparticles stabilized by the plant extract. Mater Sci Semicond Process. 2015;40:123–9. doi: 10. 1016/j.mssp.2015.05.037.
- [51] Scherrer P. Bestimmung der Größe und der inneren Struktur von Kolloidteilchen mittels Röntgenstrahlen. Nachrichten von der Ges der Wissenschaften zu Göttingen, Mathematisch-Physikalische Kl. 1918:26:98–100.
- [52] Kuzmin A, Kalinko A, Evarestov R. First-principles LCAO study of phonons in NiWO4. Open Phys. 2011;9:502–9. doi: 10.2478/s11534-010-0091-z.
- [53] Azizi S, Asadpour-Zeynali K. Electrochemical synthesis of tungstate bimetallic nanoparticles with application in electrocatalytic determination of paracetamol. ChemistrySelect. 2022;7:e202104548. doi: 10.1002/slct.202104548.
- [54] Leeladevi K, Arunpandian M, Vinoth Kumar J, Chellapandi T, Mathumitha G, Lee J-W, et al. CoWO4 decorated ZnO nanocomposite: efficient visible-light-activated photocatalyst for mitigation of noxious pollutants. Phys B Condens Matter. 2022;626:413493. doi: 10.1016/j.physb.2021.413493.
- [55] Tauc J. Optical Properties of Solids. In: Ables A, editor. North-Holland, Amsterdam; 1970.
- [56] Finčur NL, Krstić JB, Šibul FS, Šojić Dv, Despotović VN, Banić ND, et al. Removal of alprazolam from aqueous solutions by heterogeneous photocatalysis: Influencing Factors, intermediates, and products. Chem Eng J. 2017;307:1105–15. doi: 10.1016/j.cej.2016. 09 008
- [57] Shekofteh-Gohari M, Habibi-Yangjeh A. Combination of CoWO 4 and Ag 3 VO 4 with Fe 3 O 4/ZnO nanocomposites: Magnetic photocatalysts with enhanced activity through p-n-n heterojunctions under visible light. Solid State Sci. 2017;74:24–36. doi: 10.1016/ j.solidstatesciences.2017.10.001.
- [58] de Oliveira ALM, Ferreira JM, Silva MRS, de Souza SC, Vieira FTG, Longo E, et al. Influence of the Thermal Treatment in the Crystallization of NiWO4 and ZnWO4. J Therm Anal Calorim. 2009;97:167–72. doi: 10.1007/s10973-009-0244-8.
- [59] Pandey PK, Bhave NS, Kharat RB. Structural, Optical, Electrical and Photovoltaic Electrochemical Characterization of Spray Deposited NiWO4 Thin Films. Electrochim Acta. 2006;51:4659–64. doi: ELECTACTA.2005.12.042">10.1016/J.ELECTACTA.2005.12.042.
- [60] Murcia MD, Gómez M, Gómez E, Gómez JL, Christofi N. Photodegradation of Congo Red Using XeBr, KrCl and Cl2 Barrier Discharge Excilamps: A Kinetics Study. Desalination. 2011;281(1):364–71. doi: 10.1016/J.DESAL.2011.08.011.
- [61] Güy N, Özacar M. The Influence of Noble Metals on Photocatalytic Activity of ZnO for Congo Red Degradation. Int J Hydrog Energy. 2016;41:20100–12. doi: 10.1016/j.ijhydene.2016.07.063.
- [62] Ahmed Y, Yaakob Z, Akhtar P. Degradation and mineralization of methylene blue using a heterogeneous photo-fenton catalyst under visible and solar light irradiation. Catal Sci Technol. 2016;6:1222–32. doi: 10.1039/C5CY01494H.

- [63] Botsa SM, Jagadeesh Babu M, Suresh P, Kalyani P, Venkateswararao B, Muralikrishna R. Spherical NiWO4-reduced graphene oxide nanocomposite for effective visible light driven photocatalytic activity for the decolourisation of organic pollutants. Arab J Chem. 2020;13(11):8489–97. doi: 10.1016/J.ARABJC.2020. 09.017.
- [64] Pirhashemi M, Habibi-Yangjeh A. ZnO/NiWO4/Ag2CrO4 nanocomposites with p-n-n heterojunctions: Highly improved activity for degradations of water contaminants under visible light. Sep Purif Technol. 2018;193:69–80. doi: 10.1016/J.SEPPUR.2017.11.007.
- [65] Habibi-Yangjeh A, Shekofteh-Gohari M. Novel magnetic Fe3O4/ ZnO/NiWO4 nanocomposites: Enhanced visible-light photocatalytic performance through p-n heterojunctions. Sep Purif Technol. 2017;184:334–46. doi: 10.1016/J.SEPPUR.2017.05.007.
- [66] Prabavathi SL, Govindan K, Saravanakumar K, Jang A, Muthuraj V. construction of heterostructure CoWO4/g-C3N4 nanocomposite as an efficient visible-light photocatalyst for norfloxacin degradation. J Ind Eng Chem. 2019;80:558–67. doi: 10.1016/j.jiec.2019.08.035.
- [67] Mohan S, Subramanian B. A strategy to fabricate bismuth ferrite (BiFeO3) nanotubes from electrospun nanofibers and their solar light-driven photocatalytic properties. RSC Adv. 2013;3:23737. doi: 10.1039/c3ra44085k.
- [68] Aazam ES. Degradation of methylene blue dye under visible light using silver/calcium hydroxide nanospheres. Desalin Water Treat. 2018;104:330–7. doi: 10.5004/DWT.2018.21906.
- [69] Frias Batista LM, Meader VK, Romero K, Kunzler K, Kabir F, Bullock A, et al. Kinetic Control of [AuCl4]- photochemical reduction and gold nanoparticle size with hydroxyl radical scavengers. J Phys Chem B. 2019;123(33):7204–13.
- [70] Bhagwat UO, Wu JJ, Asiri AM, Anandan S. Photocatalytic degradation of congo red using PbTiO 3 nanorods synthesized via a sono-chemical approach. ChemistrySelect. 2018;3:11851–8. doi: 10.1002/slct.201802303.
- [71] Alamelu K, Raja V, Shiamala L, Jaffar Ali BM. Biphasic TiO 2 nanoparticles decorated graphene nanosheets for visible light driven photocatalytic degradation of organic dyes. Appl Surf Sci. 2018;430:145–54. doi: 10.1016/j.apsusc.2017.05.054.
- [72] Boutra B, Güy N, Özacar M, Trari M. Magnetically separable MnFe2O4/TA/ZnO nanocomposites for photocatalytic degradation of congo red under visible light. J Magn Magn Mater. 2020;497:165994. doi: 10.1016/j.jmmm.2019.165994.
- [73] Hokonya N, Mahamadi C, Mukaratirwa-Muchanyereyi N, Gutu T, Zvinowanda C. Green synthesis of P – ZrO2CeO2ZnO nanoparticles using leaf extracts of flacourtia indica and their application for the photocatalytic degradation of a model toxic dye, congo red. Heliyon. 2022;8:e10277. doi: 10.1016/j.heliyon.2022.e10277.
- [74] Sadek Kadari A, Khane Y, Nebatti Ech-Chergui A, Popa A, Guezzoul M, Silipas D, et al. Growth, properties and photocatalytic degradation of congo red using Gd:ZnO thin films under visible light. Inorg Chem Commun. 2022;142:109626. doi: 10.1016/j.inoche. 2022.109626.
- [75] Ranjithkumar R, van Nguyen C, Wong LS, Thiruvengadam Nandagopal JG, Djearamane S, Palanisamy G, et al. Chitosan functionalized bismuth oxychloride/zinc oxide nanocomposite for enhanced photocatalytic degradation of congo red. Int J Biol Macromol. 2023;225:103–11. doi: 10.1016/j.ijbiomac.2022.11.302.